IEEE Access
Multidisciplinary | Rapid Review | Open Access Journal

Received July 14, 2020, accepted August 10, 2020, date of publication August 14, 2020, date of current version August 25, 2020.

*Digital Object Identifier 10.1109/ACCESS.2020.3016746*

# A Novel Hybrid Active Contour Model for Intracranial Tuberculosis MRI Segmentation Applications

**YUZHEN CAO[1], JIAYONG MAO[1], HUI YU[1], QINHAO ZHANG[1], HUIQUAN WANG[2], QUANLU ZHANG[3], LINGFEI GUO[4], AND FEI GAO[4]**

[1]Tianjin Key Laboratory of Biomedical Detecting Techniques and Instruments, Tianjin University, Tianjin 300072, China
[2]School of Life Sciences, Tiangong University, Tianjin 300387, China
[3]The Fourth People's Hospital of Qinghai Province, Qinghai 810007, China
[4]Shandong Medical Imaging Research Institute, Cheeloo College of Medicine, Shandong University, Jinan 250021, China

Corresponding authors: Lingfei Guo (glfsci@163.com) and Fei Gao (feigao6262@163.com)

This work was supported in part by the National Natural Science Foundation of China under Grant 81170510 and Grant 81901789, in part by the Major Science and Technology Project of Tianjin, China, under Grant 20ZXGBSY00060 and Grant 18ZXZNSY00240, in part by the Taishan Scholars Project, China, under Grant tsqn201812147, and in part by the Funding for Study Abroad Program by Shandong Province under Grant 201803059.

**ABSTRACT** This paper proposes an improved region-based active contour model for segmenting magnetic resonance imaging (MRI) images of brain tuberculosis by combining a global energy fitting term and a local energy fitting term. First, a global energy fitting term is utilized to extract global image information, which guides the evolving curve globally and approximates the image intensity inside and outside the contour. Second, a local energy fitting term is proposed to describe the intensity inhomogeneity based on the local intensity variance and the adaptive image difference. Third, an improved Fuzzy C-Means (FCM) clustering method is applied to pre-segment the MRI images to automatically track the approximate location of brain tuberculosis and provide the initial contour for the hybrid model segmentation. By combining the global and local weighting functions, a hybrid region-based model is defined. Experiments demonstrate that the proposed model provides initialization of the contours automatically and offers superior segmentation performance for brain tuberculosis MRI medical images with intensity inhomogeneity.

**INDEX TERMS** Active contour, image segmentation, intracranial tuberculosis, intensity inhomogeneity.

## I. INTRODUCTION

Intracranial tuberculosis (TB) is a serious type of central nervous system tuberculosis caused by the hematogenous spread of mycobacterium tuberculosis and accounts for 1.5%-3.2% of all tuberculosis-related deaths [1], [2], ranking 11th in its disability rate and 13th in its fatality rate. The involvement of the central nervous system (CNS) is the reason that this is one of the most serious forms of this infection and is responsible for its high mortality and morbidity [3], [4]. Additionally, the manifestations of tuberculoma and tuberculous nodules in the brain have various forms that can be difficult to differentiate from other intracranial tumors [5]. Early diagnosis of CNS TB is crucial to receiving appropriate treatment, which can reduce the risk of morbidities and mortality. Routine diagnostic techniques are usually implemented on the stage of early diagnosis. However, they usually require cultures and immunological tests of tissue and biofluids, which are time-consuming and may delay definitive management [6].

As well as conventional MRIs, various MRI sequences can not only provide additional insight into the disease but also help to quantify the disease load and differentiate neuro tuberculosis from other conditions with a similar imaging appearance and presentation [7]. The varied radiological appearances of tuberculosis in MRI images are shown in Fig. 1. Parenchymal tuberculoma is the most common form of intracranial tuberculosis, which tends to occur at the location of the grey-white matter junction due to the conglomeration and coalescence of tubercular micro-granulomas [8], [9]. Clinically, patients with this condition present with headaches, seizures, and raised intracranial tension; therefore

The associate editor coordinating the review of this manuscript and approving it for publication was Yi Zhang.

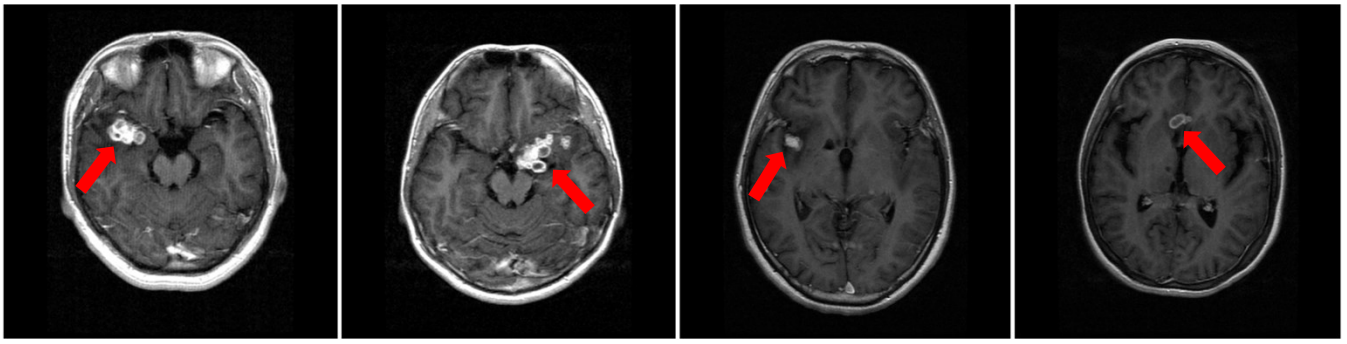

**FIGURE 1.** The varied radiological appearances of tuberculosis in MRI images.

it is necessary to extract the diseased tissues and obtain quantitative information that can be used for disease diagnosis. In recent years, the development of medical image segmentation using deep learning techniques has achieved remarkable progress [10]–[12]. Many deep learning-based models such as U-net and Fully Convolutional Network (FCN) have been applied in the field of medical image segmentation because of their excellent semantic expression ability and feature extraction which do not require manual participation in the extraction of image features and excessive preprocessing of medical images. However, it requires rich training samples to achieve successful results using deep learning techniques that remain the issues of overfitting and computation time. Since there are also privacy and ethical issues involved with medical data, medical images cannot easily be outsourced for processing by a large number of external personnel. Moreover, intracranial tuberculosis mostly occurs in Western China and underdeveloped areas where the medical image precision in local radiology departments may be limited due to a lack of human resources and poor MRI equipment conditions. This increases the difficulty of applying deep learning network segmentation due to the scarcity of tuberculosis MRI images.

Another method currently used to segment medical images is level set segmentation, which is based on the active contour model (ACM). Active contour models can be either edge-based models [13]–[17] or region-based models [18]–[22]. Edge-based models use image gradient information to control the evolution of the closed contour curve towards the target boundary. These models are generally applicable where there is a strong target boundary. However, these models are sensitive to high noise and weak boundaries. In contrast, region-based models use regional image information to guide curve evolution, thus overcoming any shortcomings due to high noise and weak boundaries [23].

Many hybrid level set algorithms integrating the local and global region intensity information have previously been implemented in MRI image segmentation. In [20], by choosing appropriate combination coefficients, Wang *et al.* proposed a model combined with a local intensity fitting term and an auxiliary global intensity fitting term to segment images with intensity inhomogeneity. Additionally, the Local Chan-Vese (LCV) model [24] proposed by Wang *et al.* introduced a difference image fitting term based on the original C-V model, which solved the problem of intensity inhomogeneity in medical images to a certain extent. However, both methods use only a fixed weight coefficient to adjust the contributions of the global and the local terms, which limits their performance on medical images with intensity inhomogeneity. In [25], Fang *et al.* proposed a novel active contour method that combines global and local region information to handle ultrasound images with noise and fuzzy edges.

In our study, a new energy function is introduced into the local and global combined fitting model. A global energy fitting term is used to extract global image information which guides the evolving curve globally, and then a local energy fitting term is used to describe the intensity inhomogeneity with local intensity variance and an adaptive difference image. The rest of the paper is structured as follows: Section 2 briefly introduces the relevant work. Section 3 presents the proposed hybrid active contour model in detail. Section 4 provides the experimental results and discussions. The conclusions of this paper are given in Section 5.

## II. RELATED WORK

### A. C-V MODEL

Chan and Vese proposed the well-known Chan-Vese (C-V) model [18] which replaces the piecewise smooth function with a piecewise constant function to approximate the intensity distribution inside and outside the initial contour by simplifying the Mumford-Shah model. Let $I(x)$ represents the original image. The energy function of the C-V model can be constructed as:

$$\begin{aligned} E_{\varepsilon}^{cv}(c_1, c_2, C) = \lambda_1 & \int_{inside(C)} |I(x) - c_1|^2 H_{\varepsilon}(\phi(x))dx \\ & + \lambda_2 \int_{outside(C)} |I(x) - c_2|^2 (1 - H_{\varepsilon}(\phi(x)))dx \\ & + \nu \int_{\Omega} \delta_{\varepsilon}(\phi(x)) H_{\varepsilon}(\phi(x))dx \end{aligned} \tag{1}$$

where $\lambda_1, \lambda_2$ and $\nu$ are nonnegative constants, $inside(C)$ and $outside(C)$ are different regions inside and outside the contour $C$, respectively, $\phi(x)$ is the level set function.

By minimizing the energy functional, the variational formulation can be obtained as:

$$\frac{\partial \phi}{\partial t} = \delta_\varepsilon(\phi)[\nu div(\frac{\nabla \phi}{|\phi|}) - \lambda_1(I(x)-c_1)^2 + \lambda_2(I(x)-c_2)^2] \quad (2)$$

where $c_1$, $c_2$ are two constants which approximate the image intensity inside and outside the contour and are defined by the Euler-Lagrange equation as:

$$\begin{cases} c_1 = \dfrac{\int I(x) H_\varepsilon(\phi(x))dx}{\int H_\varepsilon(\phi(x))dx} \\ c_2 = \dfrac{\int I(x)(1 - H_\varepsilon(\phi(x)))dx}{\int (1 - H_\varepsilon(\phi(x)))dx} \end{cases} \quad (3)$$

where $H_\varepsilon$ is the Heaviside function, $\delta_\varepsilon$ is the Dirac delta function, and they are defined by:

$$H_\varepsilon(\phi(x)) = \frac{1}{2}(1 + \frac{2}{\pi}\arctan(\frac{\phi(x)}{\varepsilon})) \quad (4)$$

$$\delta_\varepsilon(\phi(x)) = \frac{1}{\pi} \cdot \frac{\varepsilon}{\varepsilon^2 + (\phi(x))^2} \quad (5)$$

where $\varepsilon$ is a positive constant. The first two terms in (1), called the global intensity fitting energy, play a key role in encouraging the contour to evolve to the edge of the target image. The third term in (1) is the length regularizing term which regularizes the evolution curve.

One of the most attractive properties of the C-V model is that it is much less sensitive to the initialization. However, since local image information is not taken into account, the C-V model generally fails to segment images with intensity inhomogeneity.

### B. LBF MODEL

To segment medical images with intensity inhomogeneity, Li *et al.* proposed the Local Binary Fitting (LBF) model [19] to efficiently utilize local intensity information. In contrast with the C-V model, its energy function is defined as:

$$E_\varepsilon^{lbf}(f_1, f_2, C) = \int_\Omega \varepsilon dx + \nu \int_\Omega \delta_\varepsilon(\phi(x)) H_\varepsilon(\phi(x))dx + \mu \frac{1}{2}\int_\Omega (|\nabla\phi| - 1)^2 dx \quad (6)$$

where $\nu$ and $\mu$ are nonnegative constants. The first term in (6) is the local intensity fitting energy. The second term in (6) is the length regularizing term which adjusts the length of the zero-level set to derive a smooth contour and the last term in (6) is the distance regularizing term which ensures that the contours evolve steadily. The local intensity fitting energy is obtained by:

$$\varepsilon(\phi, f_1, f_2) = \sum_{i=1}^{2} \lambda_i \int_\Omega K_\sigma(x-y)|I(y) - f_i(x)|^2 M_i(\phi)dy \quad (7)$$

where $\lambda_i (i = 1, 2)$ are nonnegative constants, $M_1(\phi) = H_\varepsilon(\phi)$, $M_2(\phi) = 1 - H_\varepsilon(\phi)$, $K_\sigma$ is a Gaussian kernel with standard deviation $\sigma$, $I(y)$ represents the original image, $f_i(x)(i = 1, 2)$ are the two local fitting functions that locally approximate the intensities inside and outside the contour. They are defined by the Euler-Lagrange equation as:

$$\begin{cases} f_1(x) = \dfrac{K_\sigma(x) * (H_\varepsilon(\phi(x))I(x))}{K_\sigma(x) * H_\varepsilon(\phi(x))} \\ f_2(x) = \dfrac{K_\sigma(x) * ((1 - H_\varepsilon(\phi(x)))I(x))}{K_\sigma(x) * (1 - H_\varepsilon(\phi(x)))} \end{cases} \quad (8)$$

Due to the introduction of the kernel function, the LBF model can effectively handle medical images with intensity inhomogeneity. However, this model is sensitive to the contour initialization since its localization property may lead to the model becoming trapped in local minima.

### C. LGGIF MODEL

To integrate the local and global intensity information of the medical images effectively, an improved active contour model was proposed in [22]. The energy functional based on the local and global Gaussian intensity fitting energy (LGGIF) is defined as:

$$\begin{aligned} F^{LGGIF}(\phi, d_1, d_2, f_1, f_2) = {} & wF^{GGIF}(\phi, d_1, d_2) \\ & + (1 - w)F^{LIF}(\phi, f_1, f_2) \\ & + \nu \int |\nabla H(\phi(x))|dx \\ & + \mu \frac{1}{2}\int_\Omega (|\nabla\phi| - 1)^2 dx \end{aligned} \quad (9)$$

where $\nu$ and $\mu$ are nonnegative constants, $w$ is the scaling factor that determined the proportion in the local fitting energy $F^{LIF}$ and the global fitting energy $F^{GGIF}$. The last two terms in (9) are length regularizing term and distance regularizing term which are equivalent to the last two terms in (6). The local fitting term $F^{LIF}$ can attract the contour to stop at the true image edges, which is the same as (7). However, the global Gaussian fitting term $F^{GGIF}$ is based on the statistical numerical function and level set method, which is defined as:

$$F^{GGIF}(\phi, d_1, d_2) = \sum_{i=1}^{2} \lambda_i \int_\Omega |I(x) * K_\sigma - I(x) - d_i|M_i(\phi)dy \quad (10)$$

where $K_\sigma$ is Gaussian kernel operator, $\lambda_i (i = 1, 2)$ are nonnegative constants, $M_i(\phi)(i = 1, 2)$ are the same as those in (7), $I(x)$ represents the original image, $d_i (i = 1, 2)$ are the average intensities of $(I(x) * K_\sigma - I(x))$ inside and outside of the contour.

The original image was replaced with the difference image which was obtained by the Gaussian convolution image in the evolution equation. In addition, the average intensity of the difference image inside and outside the contour was also replaced with the average intensity of the original image during the level set evolutionary process. However, it is not enough to segment tuberculosis MRI images just by using the global Gaussian fitting energy.

## III. MATERIALS AND METHODS

### A. MATERIALS

A total of 396 tuberculosis medical images from 22 clinical subjects were acquired using a Signa HDxt 1.5T superconducting magnetic resonance scanner equipped with a standard 8-channel combined head-and-neck coil from the 4th People's Hospital of Qinghai Province, China. All images were acquired using conventional pulse sequences and axial scanning, and spanned the area between the parietal skull to the foramen magnum, with voxel resolutions of 0.45 mm × 0.45 mm in the axial plane and 5.00 mm in the z-direction. The contrast-enhanced T1-weighted images with slices of size 512 × 512 pixels were extracted for the experimental data, which were injected with contrast agent Gd-DTPA targeting angiograph. The distribution of the entire dataset is illustrated in Table 1.

**TABLE 1. The distribution of the entire dataset.**

| Types of tuberculosis | Number of patients | Number of images |
|---|---|---|
| Meningeal tuberculosis | 8 | 147 |
| Brain parenchymal tuberculosis | 10 | 163 |
| Mixed intracranial tuberculosis | 4 | 86 |
| Total number | 22 | 396 |

The results were obtained via Matlab2018a on a PC with an Intel Core CPU 2.50 and 8 GB of RAM. The study was performed in accordance with the Declaration of Helsinki and was approved by the institutional review board of the Fourth People's Hospital of Qinghai Province (QSYL2019:04). Written informed consent was obtained from all subjects.

### B. PRIOR TUBERCULOSIS SEGMENTATION

Since medical images can be disturbed by random noise during the acquisition process, noise should be removed from the brain tuberculosis MRIs before segmentation. A non-linear diffusion filter [26] was adopted to remove unwanted noise, which can enhance the uniformity of the image intensity while preserving the textural detail and boundaries. Additionally, the extra-cerebral tissues in the brain contain fat, skull, and other epidermal tissues which have an intensity that is similar to a tumor. Therefore, a region growing algorithm based on morphology is required to remove the extra-cerebral tissues.

To automatically track the approximate location of the brain tuberculosis and provide the initial contour that can be used for the subsequent segmentation, a Fuzzy C-Means (FCM) clustering method based on a 2-D histogram [27] was used to pre-segment the images. This method utilizes constrained attributes between pixel neighborhoods to establish the clustering objective function containing the neighborhood information and then iteratively updates the clustering center matrix by calculating the probability of occurrence of the diagonal elements in the 2-D histogram. The new objective

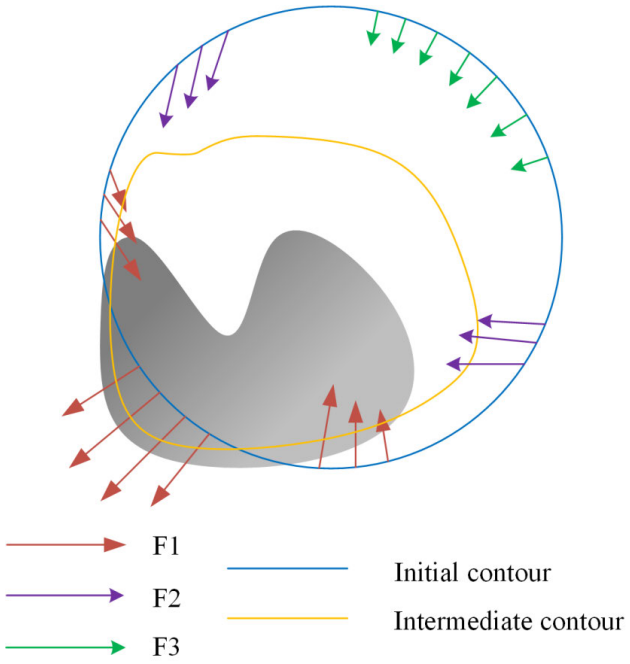


**FIGURE 2. Influence of the three fitting forces $F_1$, $F_2$ and $F_3$ during the curve evolution.**

function is defined as:

$$J_f = \sum_{k=1}^{c} \sum_{i=0}^{L-1} h(i)[\mu_{ki}]^m \, \|x_i - v_k\|^2 \tag{11}$$

where $h(i)$ is the occurrence probability of the diagonal elements in the 2-D histogram which is composed of pixels and their eight neighborhood pixels on the images, $c$ and $L$ represent the number of clusters and grayscale levels, respectively, $\mu_{ki}$ represents the membership degree of the $i$th pixel belonging to the $k$th cluster. $\|\|$ denotes the Euclidean norm. The parameter $m(m > 1)$ is a weighting exponent for each fuzzy membership that determines the amount of fuzziness of the resulting partition. $x_i$ represents the gray value of the $i$th pixel and $v_k$ denotes the center of the $k$th cluster. So $\|x_i - v_k\|^2$ represents the Euclidean distance between the $i$th pixel and the $k$th cluster. Equation (11) can be minimized using the Lagrange multiplier method which updates the cluster center $v_k^{(b)}$ and the membership function $\mu_{ki}^{(b)}$ as:

$$v_k^{(b)} = \frac{\sum_{i=0}^{L-1} h(i)(\mu_{ki}^{(b)})^m x_i}{\sum_{i=0}^{L-1} h(i)(\mu_{ki}^{(b)})^m} \quad (1 \le k \le c) \tag{12}$$

$$\mu_{ki}^{(b)} = \frac{1}{\sum_{l=1}^{c} (\frac{d_{ik}}{d_{il}})^{2/(m-1)}} \tag{13}$$

where $d_{ik} = \|x_i - v_k\|$.

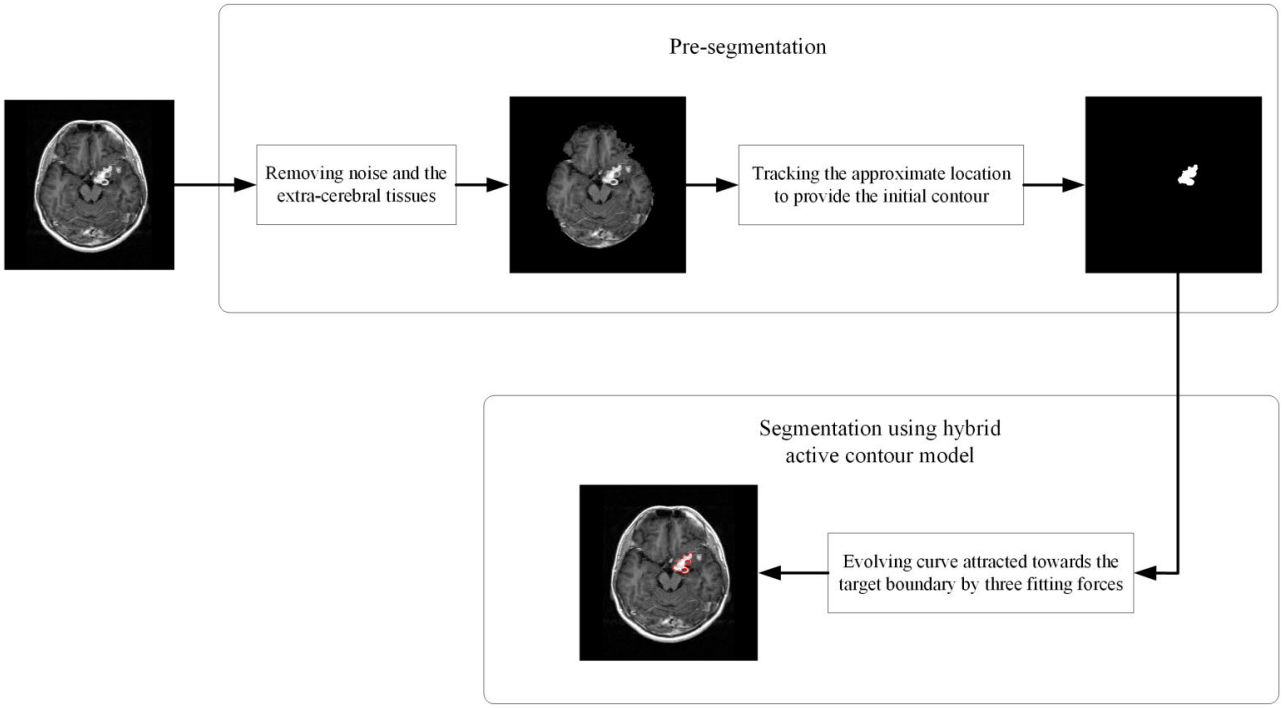


**FIGURE 3.** The block diagram of the proposed model.

### C. HYBRID ACTIVE CONTOUR MODEL

As discussed in Section II, the C-V model and the LBF model have both advantages and disadvantages when segmenting medical images. Therefore, inspired by the LGGIF model, we propose a novel hybrid active contour model that uses both global and local fitting energy. Unlike the LGGIF model, the local intensity fitting variance and adaptive difference image are introduced into the energy function to describe the intensity variation of the target region. The energy function used in our proposed model can be computed as:

$$\begin{aligned} E_\varepsilon(f_1, f_2, C) = \alpha \cdot \varepsilon^{gif} + \varepsilon^{lif} \\ + \nu \int_\Omega \delta_\varepsilon(\phi(x)) H_\varepsilon(\phi(x)) dx \\ + \mu \frac{1}{2} \int_\Omega (|\nabla \phi| - 1)^2 dx \end{aligned} \tag{14}$$

where $\alpha$ is a positive constant ($0 \le \alpha \le 1$) referred to as the fitting energy weight factor.

The last two terms in (14) are the length regularizing term and the distance regularizing term, where $\nu$ and $\mu$ are both nonnegative constants which are equivalent to the last two terms in (6). Additionally, the energy function $\varepsilon^{gif}$ which is the same as the first two terms in (1), referred to as the global fitting energy term, is constructed as:

$$\begin{aligned} \varepsilon^{gif}(\phi, c_1, c_2) = \lambda_1 \int_\Omega |I(x) - c_1|^2 H_\varepsilon(\phi(x)) dx \\ + \lambda_2 \int_\Omega |I(x) - c_2|^2 (1 - H_\varepsilon(\phi(x))) dx \end{aligned} \tag{15}$$

The second term in (14) is referred to as the local fitting energy term and represents the local region-based intensity information. Its energy function is defined as:

$$\begin{aligned} \varepsilon^{lif}(\phi, f_1, f_2) = \omega \int_\Omega (I' - I)^2 dx \\ + (1 - 2\omega) \int_\Omega \sigma_1^2(x) H_\varepsilon(\phi(x)) dx \\ + (1 - 2\omega) \int_\Omega \sigma_2^2(x) (1 - H_\varepsilon(\phi(x))) dx \end{aligned} \tag{16}$$

where $\omega \in [0, 0.5]$ is the adaptive weighting function. The first term of (16) estimates the similarity between the local adaptive image $I'$ and the original image $I$. In the second term, $\sigma_i^2(x)(i = 1, 2)$ are two local fitting functions that approximate the local intensity variance in the field of the Gaussian kernel inside and outside the contour. The local adaptive image $I'$ and the local intensity variance $\sigma_i^2(x)$ $(i = 1, 2)$ can be expressed as:

$$I' = f_1(x) H_\varepsilon(\phi(x)) + f_2(x)(1 - H_\varepsilon(\phi(x))) \tag{17}$$

$$\begin{cases} \sigma_1^2(x) = \dfrac{K_\sigma(x) * ((I - f_1(x))^2 H_\varepsilon(\phi(x)))}{K_\sigma(x) * H_\varepsilon(\phi(x))} \\ \sigma_2^2(x) = \dfrac{K_\sigma(x) * ((I - f_2(x))^2 (1 - H_\varepsilon(\phi(x))))}{K_\sigma(x) * (1 - H_\varepsilon(\phi(x)))} \end{cases} \tag{18}$$

where $K_\sigma$ is a Gaussian kernel with standard deviation $\sigma$, $f_i(x)(i = 1, 2)$ are the two local fitting functions that locally approximate the intensities inside and outside the contour, which have been defined in (8). For a given level set function, the energy function can be optimized by calculating

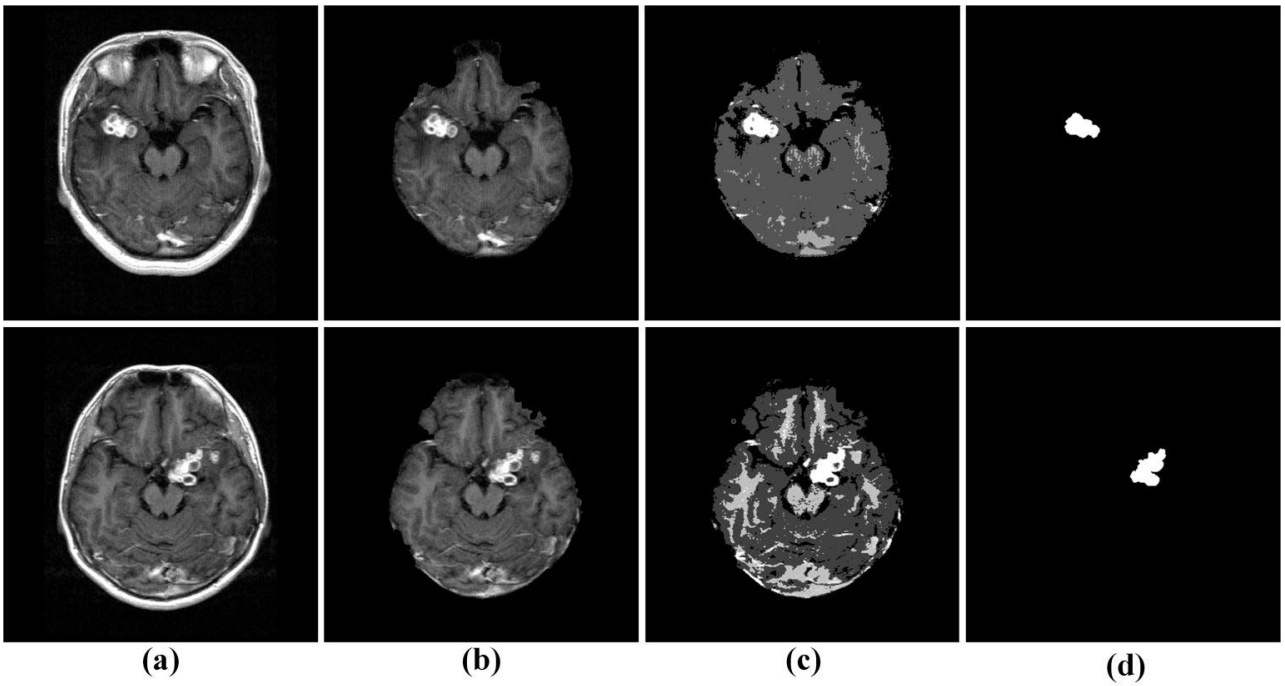


**FIGURE 4.** Pre-segmentation results. (a) Original brain tuberculosis medical images. (b) After de-noising and removal of extra-cerebral tissues. (c) The results of the improved FCM clustering method. (d) After tracking the approximate location of the brain tuberculosis.

$c_1, c_2, f_1, f_2$ and $\sigma_1^2, \sigma_2^2$ and solving the gradient descent flow equation:

$$\begin{aligned}\frac{\partial \phi}{\partial t} &= \delta_\varepsilon(\phi)(F_1 + F_2 + F_3) \\ &\quad + \nu\delta_\varepsilon(\phi) div(\frac{\nabla\phi}{|\nabla\phi|}) \\ &\quad + \mu(\nabla^2\phi - div(\frac{\nabla\phi}{|\nabla\phi|}))\end{aligned} \tag{19}$$

where $F_1, F_2$ and $F_3$ are the three fitting forces which are defined as:

$$\begin{cases} F_1 = (1-2\omega)(\sigma_1^2(x) - \sigma_2^2(x)) \\ F_2 = 2\omega(I' - I)(f_1(x) - f_2(x)) \\ F_3 = \alpha(-\lambda_1|I(x) - c_1|^2 + \lambda_2|I(x) - c_2|^2) \end{cases} \tag{20}$$

These three forces each play different roles on the curve evolution as illustrated by example in Fig. 2. At the beginning of the evolution, the evolving curve is far away from the object boundary. As a result, force $F_3$ is dominant which accelerates the contour convergence towards the target boundary. As the curve propagates, the distance between the evolving curve and the object boundary narrows so force $F_2$ becomes dominant. The adaptive weighting function $\omega$ in (16) also plays an important role in the curve evolution while the contour continues to converge stably based on image similarity. When the evolving curve reaches the object boundary, force $F_1$ dominates, which attracts the curve towards the object boundary based on the local intensity variance information. The adaptive weighting function $\omega$ is given as:

$$\omega = \frac{1}{2(1 + \exp[-\int_\Omega (f_1(x) - f_2(x))^2 dx])} \tag{21}$$

where exp denotes the exponential function. As a matter of convenience, the fixed parameters and parameters to be solved during optimization are illustrated in Table 2. The block diagram of our method is illustrated in Fig. 3 which shows the whole process pipeline and intermediate result.

## IV. RESULTS AND ANALYSIS

### A. EVALUATION METRICS

To evaluate the performance of the proposed model, the segmentation results for the brain tuberculosis MRI images were objectively evaluated using three metrics to measure the accuracy of the segmentation results: the Dice Similarity Coefficient (DSC), the Jaccard Similarity Coefficient (JSC) and the Conformity Similarity Coefficient (CSC). The closer the value of each of these metrics is to 1, the more accurate the segmentation. The three metrics are defined as:

$$\begin{cases} DSC = \dfrac{2\,|\Omega_1 \cap \Omega_2|}{|\Omega_1| + |\Omega_2|} \times 100\% \\ JSC = \dfrac{|\Omega_1 \cap \Omega_2|}{|\Omega_1 \cup \Omega_2|} \times 100\% \\ CSC = (3 - \dfrac{|\Omega_1| + |\Omega_2|}{|\Omega_1 \cap \Omega_2|}) \times 100\% \end{cases} \tag{22}$$

where $\Omega_1$ and $\Omega_2$ represent the segmentation results of the different active contour models and the ground truth, respectively.

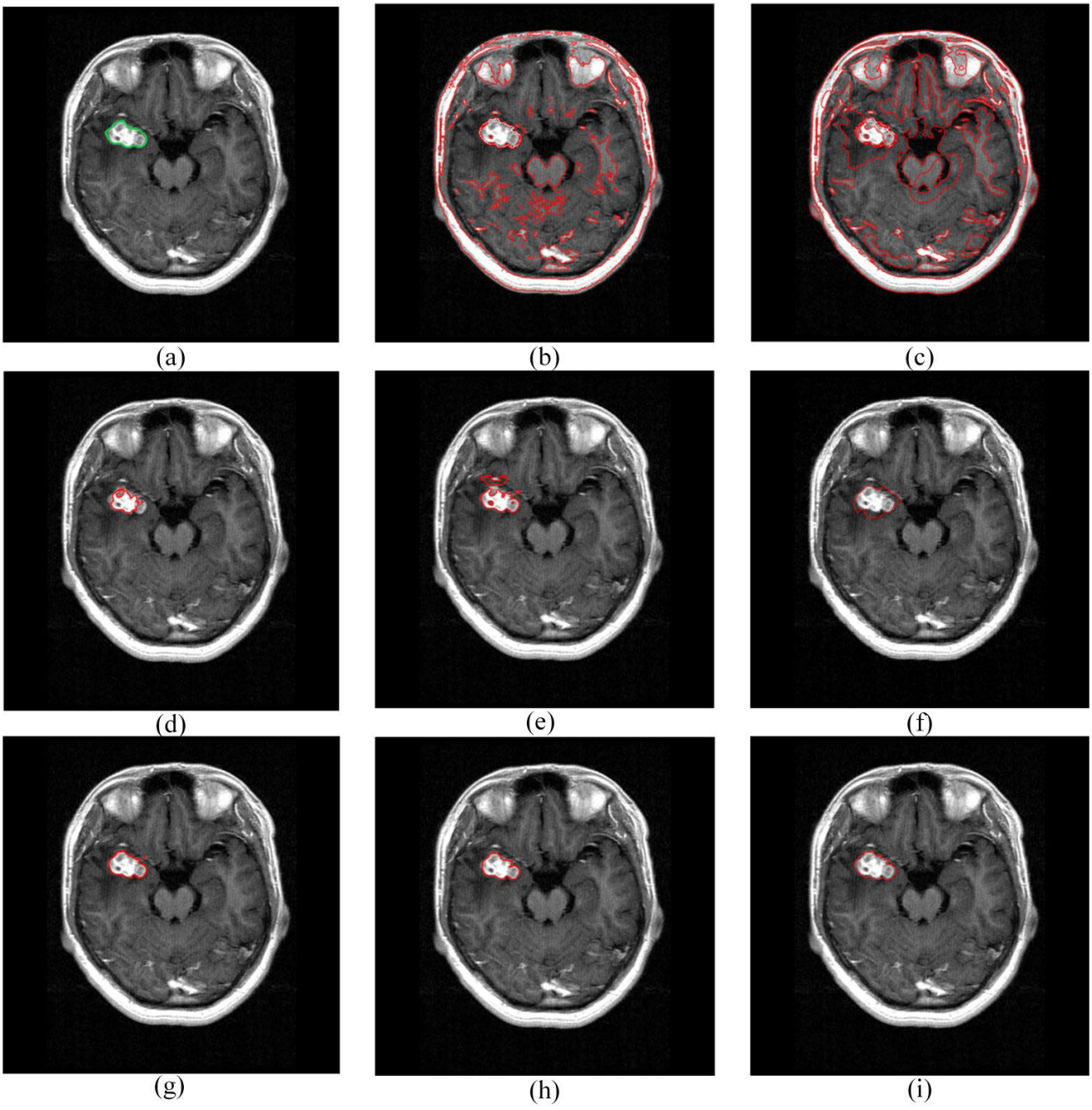


**FIGURE 5.** Segmentation results for image A using different active contour models compared with the ground truth. (a) The input image with the initial curve provided by the improved FCM method for each model; (b) C-V; (c) LBF; (d) ORACM; (e) ACM_LPF; (f) LGGIF; (g) LG_US; (h) Our method; (i) Ground truth.

To evaluate the universality of the proposed model, a hypothesis testing was performed by using the two-sample t-test which is defined as:

$$T = (\bar{X} - \bar{Y})/\sqrt{\frac{(n_1 + n_2)[(n_1 - 1)S_1^2 + (n_2 - 1)S_2^2]}{n_1 n_2 (n_1 + n_2 - 2)}} \quad (23)$$

where $\bar{X}$, $\bar{Y}$ represent the two sample means, $S_1^2$, $S_2^2$ represent the two sample variances, and $n_1$, $n_2$ denote the two sample sizes.

### B. PRE-SEGMENTATION RESULTS

The pre-segmentation results for two tuberculoma samples are presented in Fig. 4 and can provide a better understanding of the image preprocessing. The original brain MRI images of tuberculosis containing random noise are displayed in Fig. 4a. Fig. 4b shows the results after de-noising and removing extra-cerebral tissues. There were five clusters chosen since the tuberculosis MRI sample images include background, gray matter, white matter, cerebrospinal fluid, and brain tuberculosis. The results of clustering and tracking the approx-

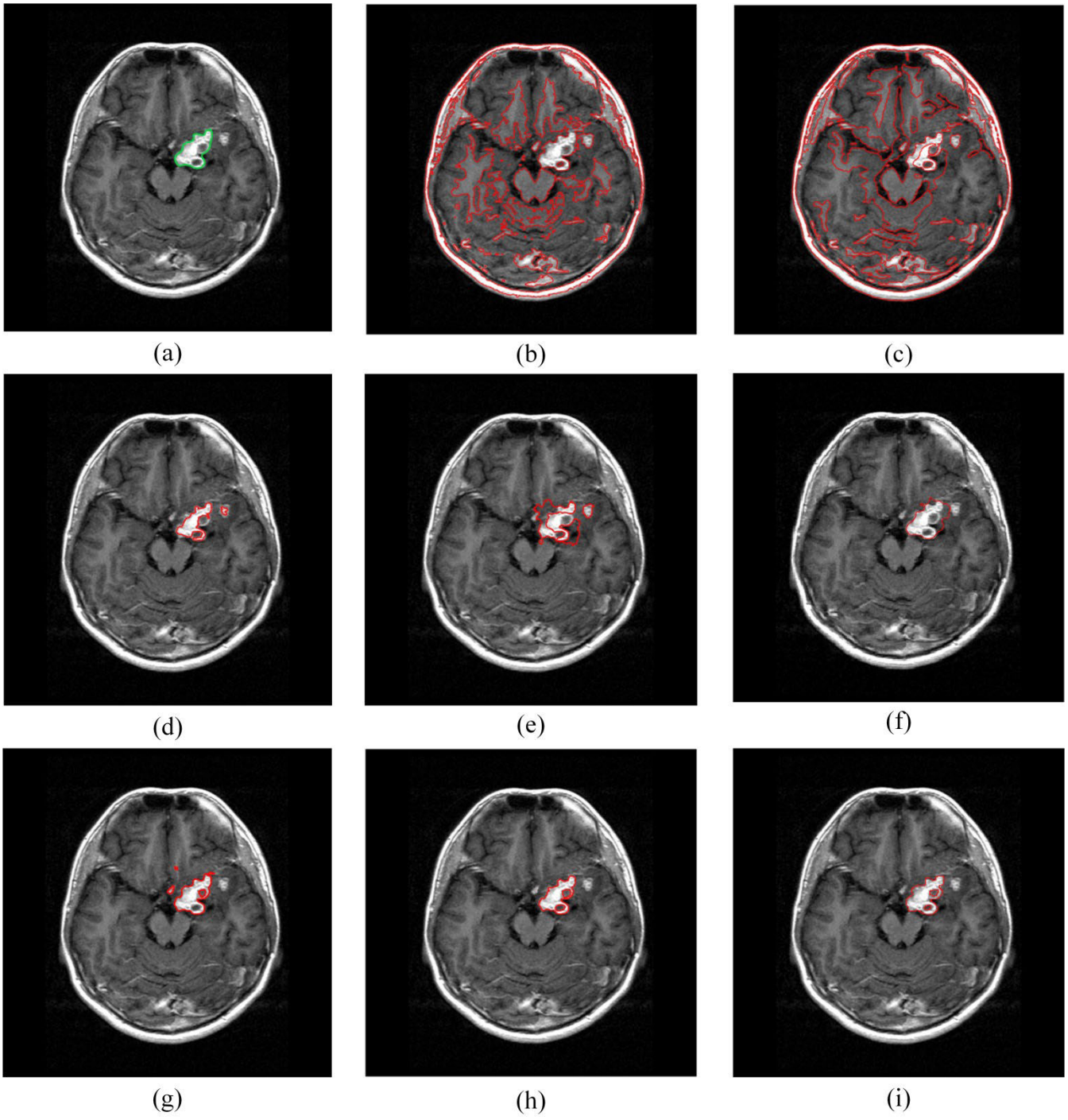


**FIGURE 6.** Segmentation results for image B using different active contour models compared with the ground truth. (a) The input image with the initial curve provided by the improved FCM method for each model; (b) C-V; (c) LBF; (d) ORACM; (e) ACM_LPF; (f) LGGIF; (g) LG_US; (h) Our method; (i) Ground truth.

imate location of the brain tuberculosis are illustrated in Fig. 4c and 4d, after using the FCM clustering method based on a 2-D histogram. Since the method utilizes constrained attributes between pixel neighborhoods to establish the clustering objective function containing the neighborhood information, the occurrence probability of the diagonal elements on the area close to the occipital lobe is indeed significantly lower $0.3\pm0.04$ than that of tuberculosis. Besides, we use the morphological operation to remove meaningless pixels and fill holes. These experimental results demonstrate the ease of selection of the initial contour for the level set segmentation.

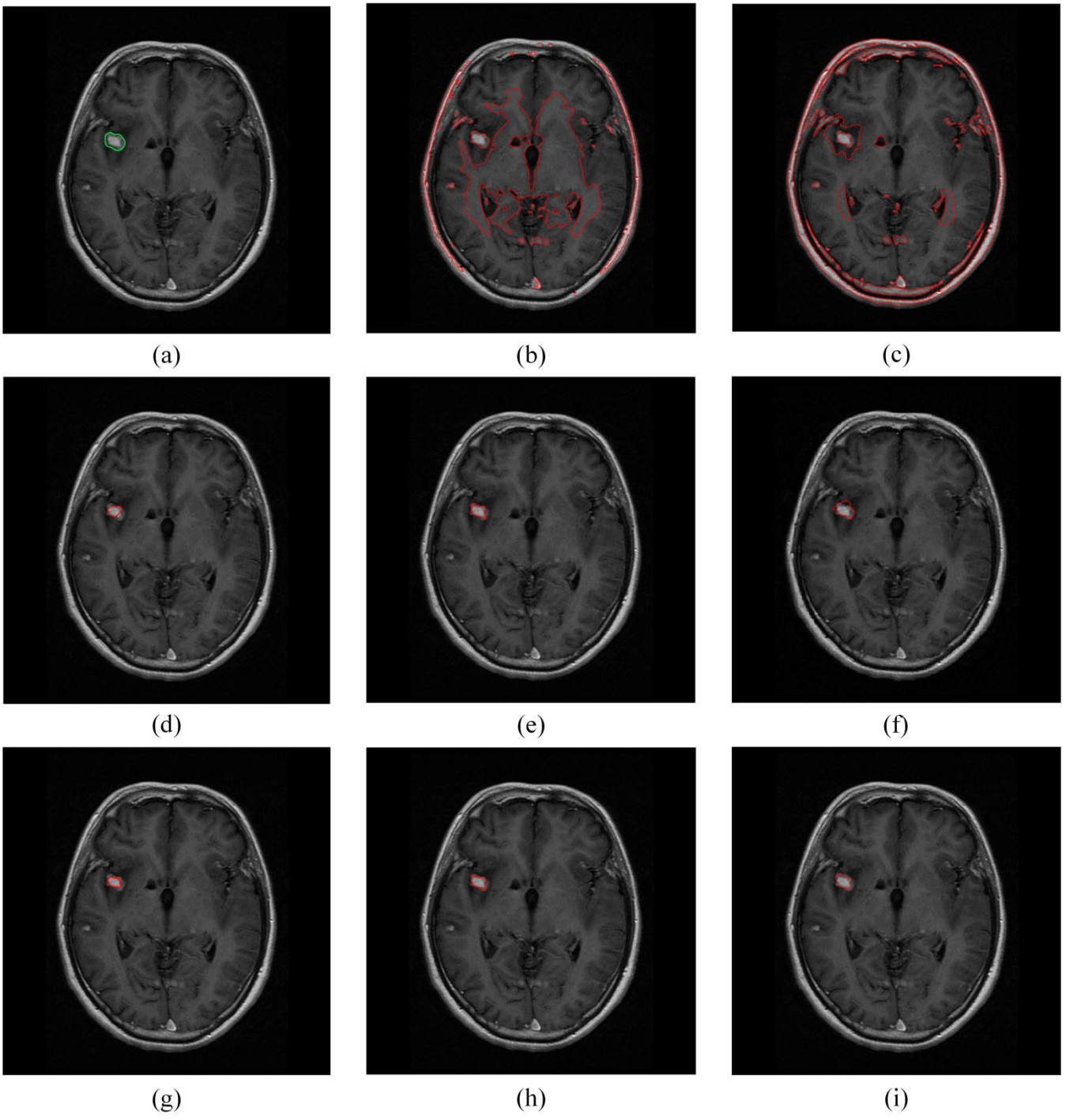


**FIGURE 7.** Segmentation results for image C using different active contour models compared with the ground truth. (a) The input image with the initial curve provided by the improved FCM method for each model; (b) C-V; (c) LBF; (d) ORACM; (e) ACM_LPF; (f) LGGIF; (g) LG_US; (h) Our method; (i) Ground truth.

### C. COMPARATIVE EVALUATION RESULTS

For comparison with other segmentation models, the default parameters were set as follows: $\lambda_1 = \lambda_2 = 1.0$, fitting energy weight $\alpha = 0.3$, time step $\Delta t = 0.1$, $\nu = 0.001 \times 255^2$, $\mu = 1.0$, $\varepsilon = 1$ and standard deviation $\sigma = 3.0$. The value of the weighting function $\omega$ was adaptively tuned during the curve evolution. Fig. 5-8 demonstrate the segmentation results for four brain tuberculosis medical images A-D from four clinical subjects using different active contour models compared with the ground truth. The input images with the initial curve provided by the improved FCM method for each model are shown in Fig. 5-8a. The results

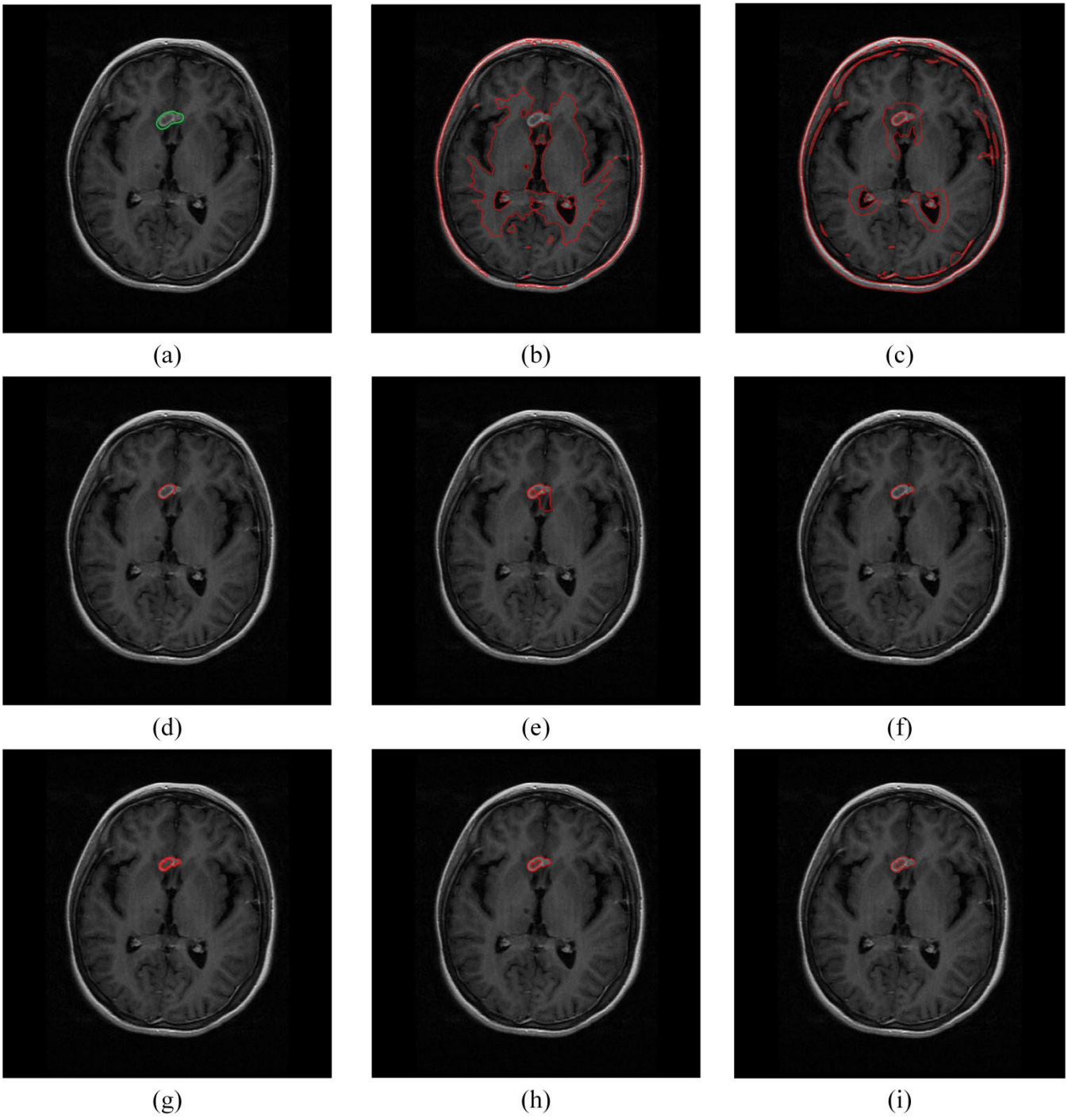


**FIGURE 8.** Segmentation results for image D using different active contour models compared with the ground truth. (a) The input image with the initial curve provided by the improved FCM method for each model; (b) C-V; (c) LBF; (d) ORACM; (e) ACM_LPF; (f) LGGIF; (g) LG_US; (h) Our method; (i) Ground truth.

of the C-V model, the LBF model, the online region-based ACM (ORACM) [28], the ACM driven by local pre-fitting energy (ACM_LPF) [29], the LGGIF model, the ACM by local and global intensity information for ultrasound image (LG_US) [25] and the proposed model are shown in Fig. 5-8b, 5-8c, 5-8d, 5-8e, 5-8f, 5-8g and 5-8h, respectively. The ground truth results are shown in Fig. 5-8i which were obtained through repeated delineation during three weeks by a well-trained radiologist with 15 years of experience. The diagnostic criteria was that only the whole tumor was covered for segmentation, avoiding adjacent vessels and the average duration between reviews of slides was one week. The mean

**TABLE 2.** Parameters in the proposed model.

| | Parameters |
|---|---|
| Fixed parameters | Nonnegative constants $\lambda_i (i=1,2)$ |
| | The fitting energy weight factor $\alpha$ |
| | Length regularizing constant $\nu$ |
| | Distance regularizing constant $\mu$ |
| | The standard deviation of Gaussian kernel $\sigma$ |
| Parameters to be solved during optimization | Constants approximating the image intensity inside and outside the contour $c_i (i=1,2)$ |
| | Local fitting functions approximating the intensities inside and outside the contour $f_i(x)(i=1,2)$ |
| | Local fitting functions approximating the local intensity variance in the field of the Gaussian kernel inside and outside the contour $\sigma_i^2(x)(i=1,2)$ |

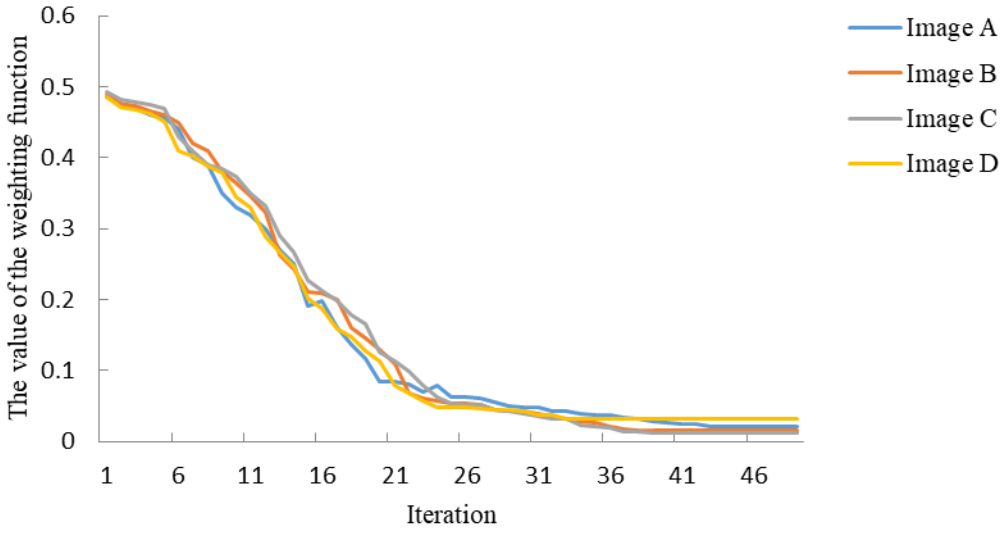


**FIGURE 9.** The values of the weighting function $\omega$ for images A-D using the proposed model.

K-value [30] was 0.83 to evaluate the intraobserver agreement which was considered very good when K-values range from 0.8 to 1. As can be seen from the segmentation results in Fig. 5-8, the C-V, LBF, ORACM, ACM_LPF, LGGIF, and LG_US provide poor segmentation of brain tuberculosis medical images since the C-V model and the ORACM model cannot handle the weak boundaries and strong noise on brain tuberculosis medical images with intensity inhomogeneity. With the LBF and ACM_LPF, it is difficult to distinguish the brain tuberculosis characteristics of the target region and their energy functions can easily become trapped in local minima. In addition, without considering the local intensity fitting variance, the LGGIF and LG_US both achieved unsatisfactory results. Compared with the above models, our method achieves better results due to the introduction of the adaptive difference image and the local intensity fitting variance. It also shows good segmentation of the inner holes in the brain tuberculoma. As the evolving curve propagates towards the boundary, the values of the weighting function $\omega$ for images A-D using our method vary as illustrated in Fig. 9 which shows that it has a downward tendency as the iteration increases. According to (22), the mean DSC, JSC, and CSC of images A-D using our method compared with the other models are presented in Fig. 10 which illustrates that the three coefficients of the proposed model are higher than the others. Furthermore, the iterations and computation time of images A-D and the average iterations and time of the entire dataset using our method compared with the other models are summarized in Table 3 which also demonstrates the efficiency of the proposed model.

Additionally, the universality of the proposed model is analyzed and evaluated by selecting all brain tuberculosis medical images and undertaking statistical analysis to obtain the mean and variance of the three coefficients which are

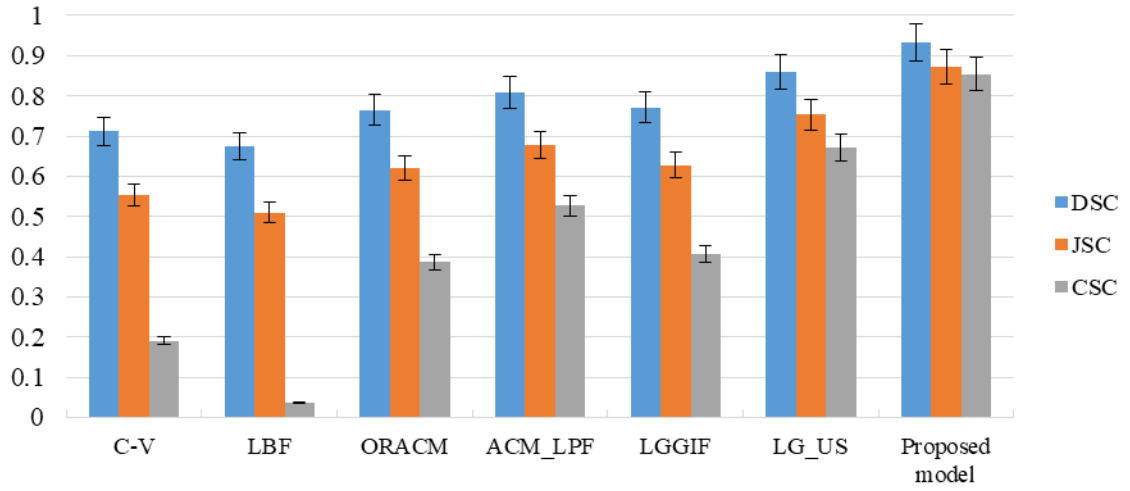


**FIGURE 10.** The mean DSC, JSC, and CSC of the images A-D using the proposed model compared with the other models.

**TABLE 3.** The iterations (Iter.) and computation time (in seconds) of the images A-D and the average iter and time of the entire dataset using our method compared with the other models.

| | Image A | | Image B | | Image C | | Image D | | | |
|---|---|---|---|---|---|---|---|---|---|---|
| | Iter. | Time | Iter. | Time | Iter. | Time | Iter. | Time | Average iter. | Average time |
| C-V | 195 | 25.533 | 210 | 27.881 | 130 | 16.432 | 110 | 14.762 | 175 | 19.423 |
| LBF | 200 | 24.715 | 210 | 25.545 | 150 | 24.131 | 150 | 23.774 | 205 | 24.951 |
| ORACM | 50 | 3.674 | 50 | 3.263 | 40 | 2.134 | 40 | 2.015 | 55 | 2.896 |
| ACM_LPF | 150 | 21.117 | 150 | 23.044 | 110 | 17.955 | 100 | 15.125 | 110 | 18.619 |
| LGGIF | 140 | 19.982 | 150 | 19.648 | 125 | 18.951 | 100 | 16.518 | 150 | 20.384 |
| LG_US | 90 | 5.068 | 100 | 3.686 | 70 | 3.429 | 65 | 2.422 | 80 | 4.164 |
| Our method | 55 | 3.544 | 60 | 3.212 | 50 | 2.661 | 45 | 2.125 | 65 | 3.265 |

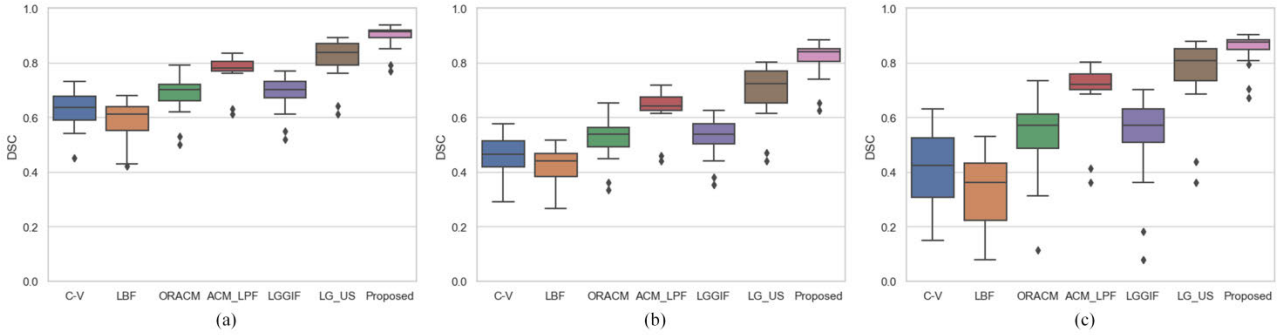


**FIGURE 11.** DSC box plots of the proposed model compared with the other models for different tuberculoma segmentation tasks. (a) Segmentation task for caseating granulomas; (b) Segmentation task for caseating granulomas with central liquefaction; (c) Segmentation task for caseating granulomas with central solidification.

summarized in Table 4. The mean values of DSC, JSC, and CSC using the proposed model are the highest of all ACMs. These results indicate that the segmentation results of the proposed model are more accurate than the other models. Furthermore, to evaluate the universality of the proposed model, we perform a hypothesis testing on the three metrics to identify the significance of the coefficients using the two-sample t-test method. According to (23), for a signif-

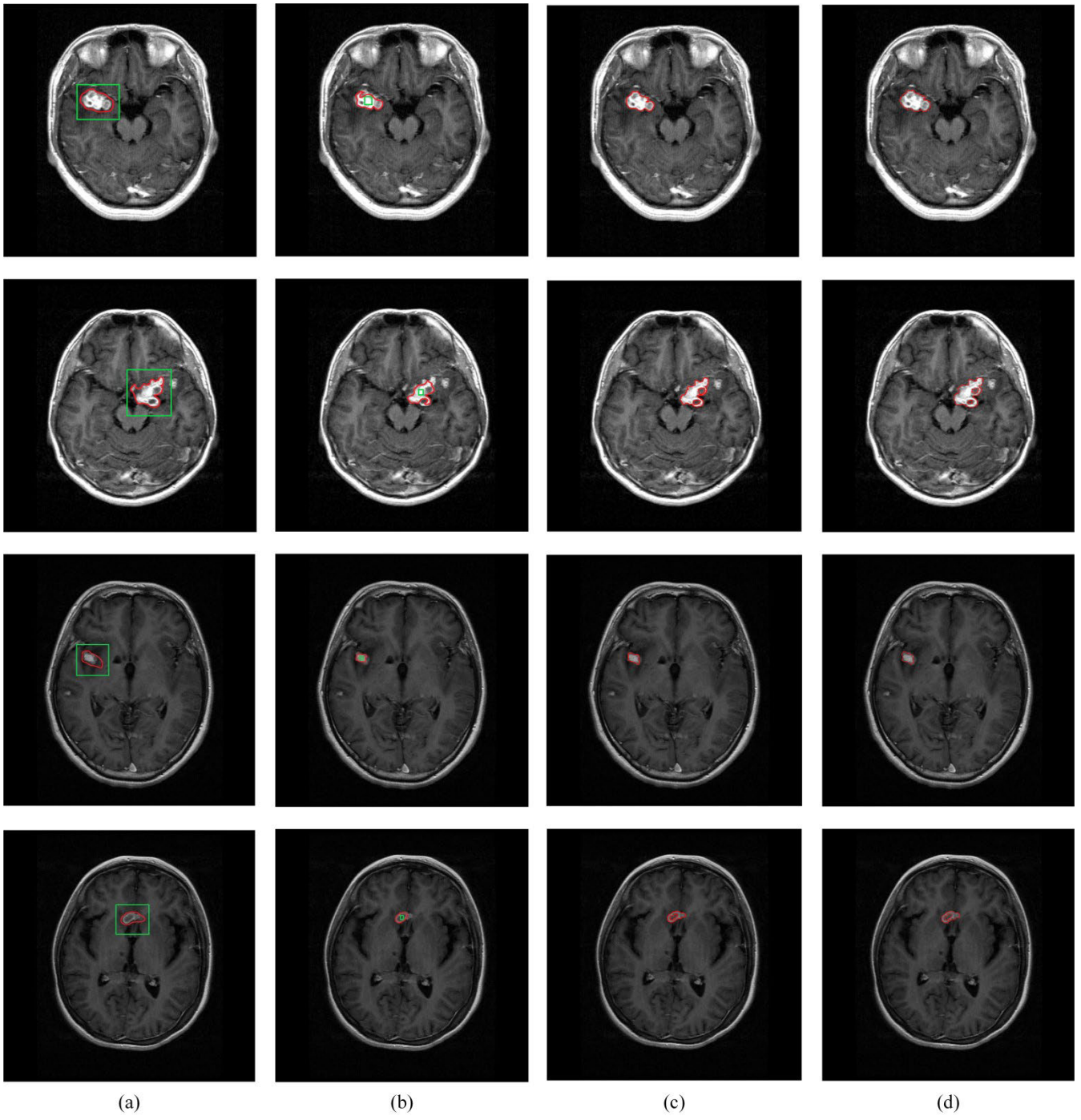


**FIGURE 12.** The segmentation results without the initial curve provided by the improved FCM method. (a) Initial curve outside tuberculosis; (b) Initial curve inside tuberculosis; (c) Proposed model; (d) Ground truth.

icance level $\alpha = 0.05$, the results demonstrate that our method shows statistically significant improvement ($p < 0.05$) compared with the other models, which means the proposed model has strong feasibility and efficiency in real clinical application.

Fig. 11 shows the DSC box plots of the proposed model compared with the other models for different tuberculoma segmentation tasks, categorized as caseating granulomas, caseating granulomas with central liquefaction, and caseating granulomas with central solidification. As shown in Fig. 11, the proposed model has the highest DSC values with the most concentrated distribution of all ACMs. Additionally, the caseating granuloma has the greatest DSC median of the three DSC box plots using the proposed model, which may

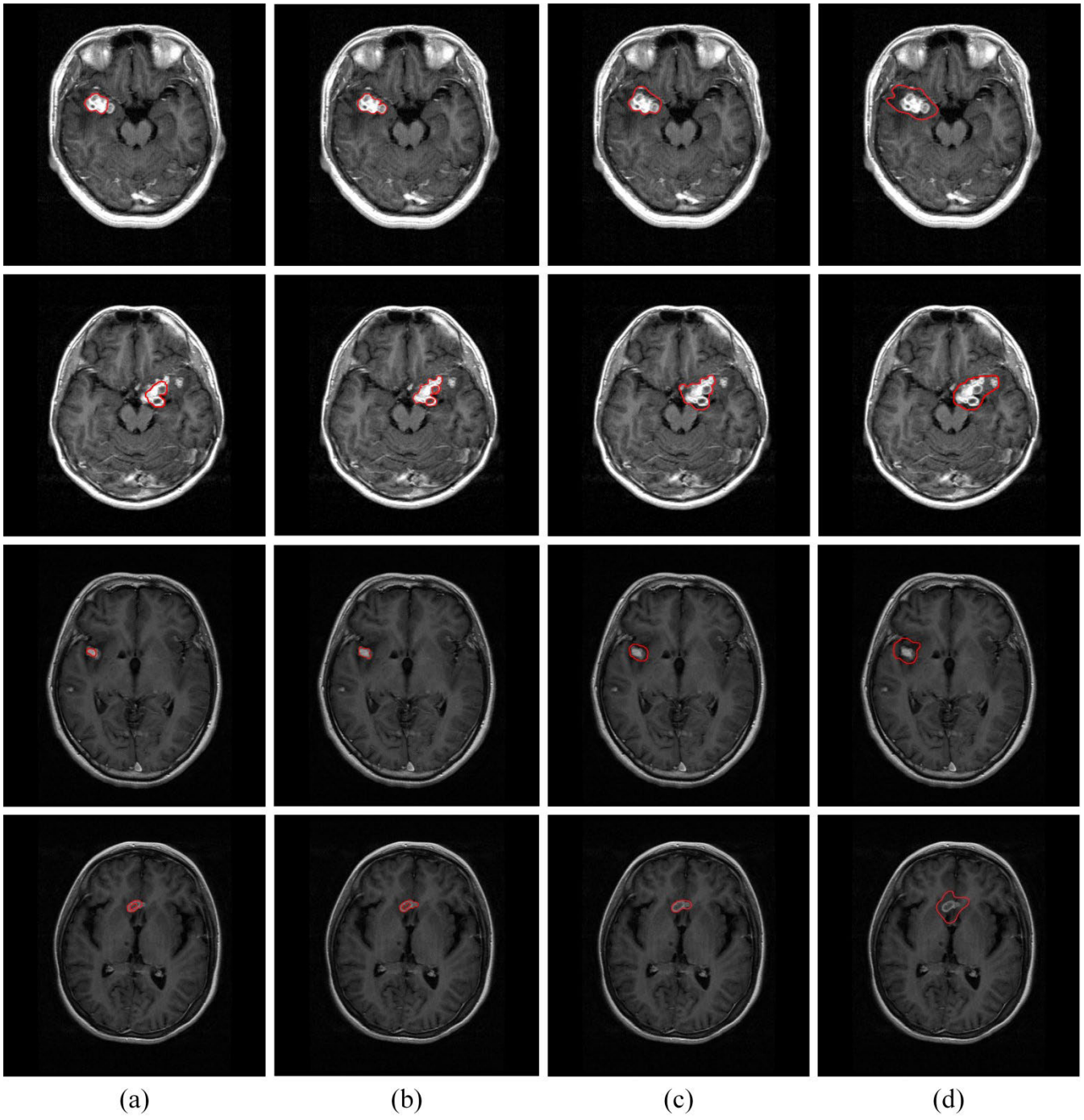


**FIGURE 13.** Comparison of the proposed model using different parameters $\alpha$. (a) $\alpha = 0.1$; (b) $\alpha = 0.3$; (c) $\alpha = 0.5$; (d) $\alpha = 0.7$.

be due to the homogeneity of the annular center and the surrounding tissues on the contrast-enhanced T1-weighted images.

To further validate the effectiveness of the pre-segmentation, the segmentation results without the initial curve provided by the improved FCM method are illustrated in Fig. 12. Compared with the results of the proposed model in Fig. 12c, the results of initial curves outside and inside tuberculosis can not converge to the object boundaries accurately, which are shown in Fig. 12a and 12b, respectively.

In recent years, the development of medical image segmentation using deep learning techniques has achieved remarkable progress. Convolutional Neural Networks (CNN) are able to learn from examples and demonstrate state-of-the-art segmentation accuracy in medical images. However, it requires rich training samples to achieve successful results

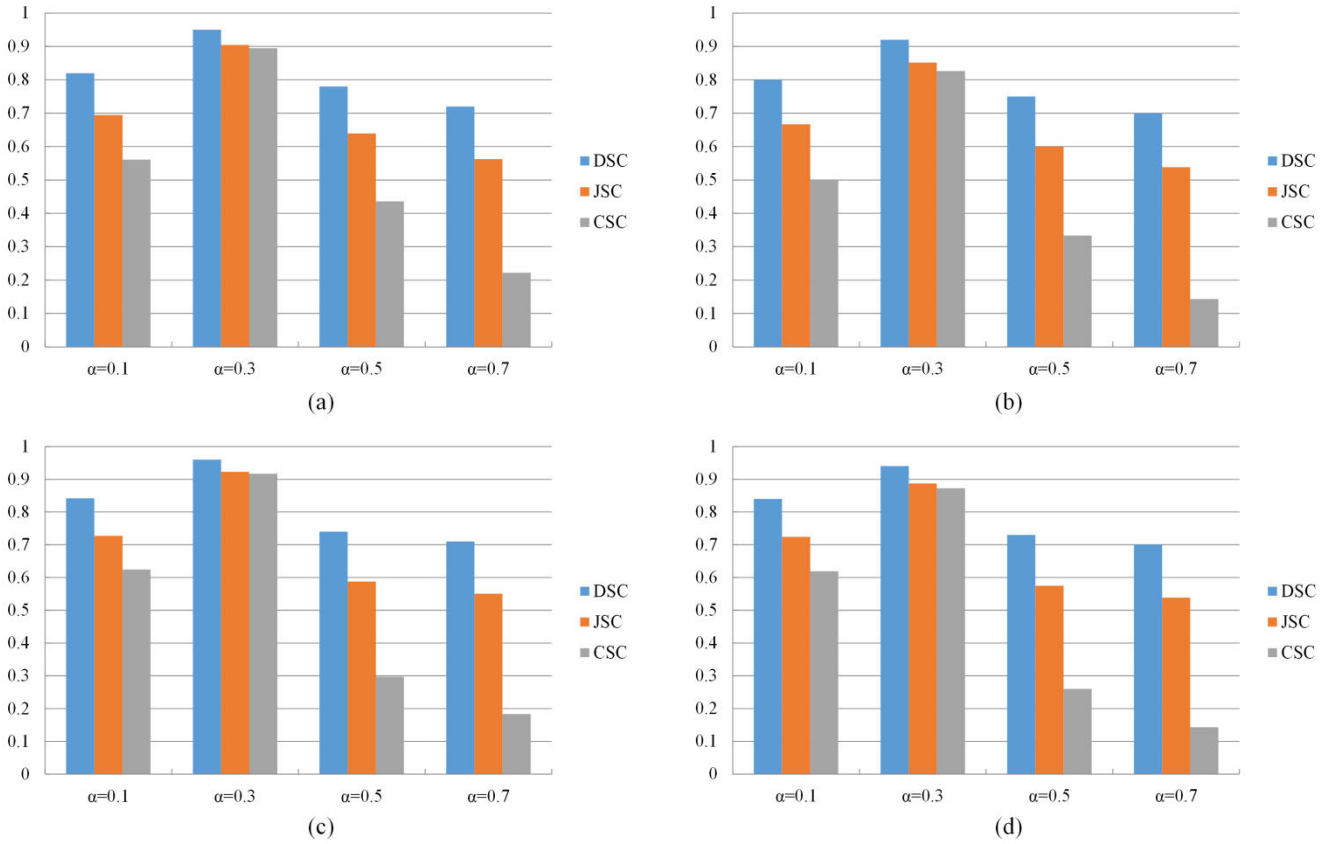


**FIGURE 14.** DSC, JSC, and CSC of the proposed model using different parameters $\alpha$ for images A-D.

**TABLE 4.** The means and standard deviations (SD) of DSC, JSC, and CSC of the entire dataset using our method compared with the other models.

| | DSC | | JSC | | CSC | |
|---|---|---|---|---|---|---|
| | Mean (%) | SD (%) | Mean (%) | SD (%) | Mean (%) | SD (%) |
| C-V | 70.08 | 0.58 | 53.94 | 1.34 | 14.61 | 1.97 |
| LBF | 66.87 | 0.41 | 50.23 | 0.98 | 0.91 | 1.54 |
| ORACM | 75.45 | 1.58 | 60.58 | 3.86 | 34.92 | 1.86 |
| ACM_LPF | 83.86 | 0.71 | 72.21 | 1.92 | 61.51 | 3.79 |
| LGGIF | 79.62 | 1.12 | 66.14 | 2.33 | 48.81 | 2.96 |
| LG_US | 87.74 | 0.85 | 78.16 | 1.81 | 72.05 | 2.34 |
| Our method | 93.56 | 0.55 | 87.90 | 1.58 | 86.23 | 2.13 |

using deep learning techniques which still remain the issues of overfitting and computation time. Xue *et al.* [31] proposed a cascaded 3D fully convolution network (FCN) to segment brain metastases (BM) by collecting 1652 patients from three hospitals and achieved the dice ratio of 0.85±0.08. It required approximately 23 hours to train the model, whereas labeling a single input image using the trained model required approximately 24 s. Additionally, Myronenko [32] proposed a semantic segmentation network for tumor subregion segmentation from 3D MRIs based on encoder-decoder architecture by using 542 cases BraTS 2018 dataset and achieved the average dice 0.86±0.04. It required approximately 2 days to train the model and the inference time is 0.4 s for a single model. Compared with the results of the above research, our method has two main advantages. Firstly, our method achieved the average dice of 0.93±0.03 and average computation time of 3.265 s, which has significant improvement in the comprehensive performance.

Secondly, our method only required six parameters to be solved during optimization which did not require time-consuming training while CNN models usually require millions of parameters and thousands of samples which sometimes need data augmentation to maintain the stability of the models.

### D. PARAMETER SELECTION RESULTS

In the following, we discuss the parameter selection of $\alpha$ which referred to as the fitting energy weight factor. Usually, a smaller value of the parameter $\alpha$ should be chosen if the medical image has strong intensity inhomogeneity. As can be seen from Fig. 13, the desired segmentation can be obtained when we set $\alpha = 0.3$ as shown in Fig. 13b. On the contrary, the segmentation results by setting the parameter $\alpha = 0.1$, 0.5, and 0.7 achieve unsatisfactory performances, which are presented in Fig. 13a, 13c, and 13d, respectively. Moreover, Fig. 14 illustrates the quantitative DSC, JSC, and CSC using different parameters $\alpha$ for images in Fig. 13. It can be seen that the highest DSC, JSC, and CSC for each image are obtained when $\alpha = 0.3$.

## V. CONCLUSION

In this paper, an active contour model segmentation algorithm based on the global and the local ACMs has been proposed to segment brain tuberculosis medical MRI images. The proposed model introduces local intensity fitting variance and adaptive difference images into the energy function. The experimental results show that the proposed model can effectively segment brain tuberculosis medical MRI images with intensity inhomogeneity. Another advantage of the proposed model is that it is fully automatic, in contrast with most other current contour segmentation approaches that require some level of user interaction. This is highly significant when there is a large volume of data to be processed.

Additionally, this model is limited as it cannot automatically segment miliary tuberculoma since it contains innumerable small noncaseating granulomas. Currently, manual delineation of the region of interest is required before the proposed model can be used to segment the local smaller nodules. This will be further studied and improved in the future. Another extension of our study is investigating methods that can be used to improve the segmentation accuracy for 3D image segmentation.

## REFERENCES

[1] M. A. Schaller, F. Wicke, C. Foerch, and S. Weidauer, "Central nervous system tuberculosis: Etiology, clinical manifestations and neuroradiological features," *Clin. Neuroradiol.*, vol. 29, no. 1, pp. 3–18, Mar. 2019.
[2] A. Yakobi, A. Z. Porterfield, J. Toman, T. Spock, N. Kapil, J. de Meyer, A. Kejner, P. Rea, N. Gleeson, B. Enicker, E. Michaelides, and Y. Saman, "HIV, tuberculosis, and otogenic intracranial sepsis: A devastating disease With a subtle presentation," *Otol. Neurotol.*, vol. 40, no. 7, pp. 704–712, Aug. 2019.
[3] J. H. Chin and F. J. Mateen, "Central nervous system tuberculosis: Challenges and advances in diagnosis and treatment," *Current Infectious Disease Rep.*, vol. 15, no. 6, pp. 631–635, Dec. 2013.
[4] J. M. Leonard, "Central nervous system tuberculosis," *Microbiol. Spectr.*, vol. 5, no. 2, pp. 331–341, Mar. 2017.
[5] A. Bleibtreu, N. Grall, J.-P. Laissy, C. Rioux, A. Strukov, S. Lariven, P. Yeni, Y. Yazdanpanah, and V. Joly, "Contribution of brain imaging to the diagnosis of intracranial tuberculoma and other brain lesions in patients presenting with miliary tuberculosis," *Médecine et Maladies Infectieuses*, vol. 48, no. 8, pp. 533–539, Dec. 2018.
[6] H. Yu, H. Wang, Y. Shi, K. Xu, X. Yu, and Y. Cao, "The segmentation of bones in pelvic CT images based on extraction of key frames," *BMC Med. Imag.*, vol. 18, no. 1, pp. 18–31, May 2018.
[7] J. S. Molton, B. A. Thomas, Y. Pang, L. K. Khor, J. Hallinan, C. M. Naftalin, J. J. Totman, D. W. Townsend, T. K. Lim, C. B. E. Chee, Y. T. Wang, and N. I. Paton, "Sub-clinical abnormalities detected by PET/MRI in household tuberculosis contacts," *BMC Infectious Diseases*, vol. 19, no. 1, pp. 83–89, Jan. 2019.
[8] G. D. Khatri, V. Krishnan, N. Antil, and G. Saigal, "Magnetic resonance imaging spectrum of intracranial tubercular lesions: One disease, many faces," *Pol. J. Radiol.*, vol. 83, pp. 524–535, Dec. 2018.
[9] H. M. Dahmoush and A. N. Pollock, "Parenchymal brain tuberculoma in a patient with sickle cell disease," *Pediatric Emergency Care*, vol. 28, no. 7, pp. 724–725, Jul. 2012.
[10] L. Wang, R. Chen, S. Wang, N. Zeng, X. Huang, and C. Liu, "Nested dilation network (NDN) for multi-task medical image segmentation," *IEEE Access*, vol. 7, pp. 44676–44685, 2019.
[11] C. Angela, W. Carolina, and C. Carlos, "Medical image segmentation using the Kohonen neural network," *IEEE Latin Amer. Trans.*, vol. 17, no. 2, pp. 297–304, Feb. 2019.
[12] J. Minnema, M. van Eijnatten, W. Kouw, F. Diblen, A. Mendrik, and J. Wolff, "CT image segmentation of bone for medical additive manufacturing using a convolutional neural network," *Comput. Biol. Med.*, vol. 103, pp. 130–139, Dec. 2018.
[13] A. Rodtook and S. S. Makhanov, "Multi-feature gradient vector flow snakes for adaptive segmentation of the ultrasound images of breast cancer," *J. Vis. Commun. Image Represent.*, vol. 24, no. 8, pp. 1414–1430, Nov. 2013.
[14] Y. Le, X. Xu, L. Zha, W. Zhao, and Y. Zhu, "Tumor boundary detection in ultrasound imagery using multi-scale generalized gradient vector flow," *J. Med. Ultrason.*, vol. 42, no. 1, pp. 25–38, Jan. 2015.
[15] K. Mu, F. Hui, X. Zhao, and C. Prehofer, "Multiscale edge fusion for vehicle detection based on difference of Gaussian," *Optik*, vol. 127, no. 11, pp. 4794–4798, Jun. 2016.
[16] C. Liu, W. Liu, and W. Xing, "A weighted edge-based level set method based on multi-local statistical information for noisy image segmentation," *J. Vis. Commun. Image Represent.*, vol. 59, pp. 89–107, Feb. 2019.
[17] A. Pratondo, C. K. Chui, and S. H. Ong, "Robust edge-stop functions for edge-based active contour models in medical image segmentation," *IEEE Signal Process. Lett.*, vol. 23, no. 2, pp. 222–226, Feb. 2016.
[18] T. F. Chan and L. A. Vese, "Active contours without edges," *IEEE Trans. Image Process.*, vol. 10, no. 2, pp. 266–277, Feb. 2001.
[19] C. Li, C.-Y. Kao, J. C. Gore, and Z. Ding, "Minimization of region-scalable fitting energy for image segmentation," *IEEE Trans. Image Process.*, vol. 17, no. 10, pp. 1940–1949, Oct. 2008.
[20] L. Wang, C. Li, Q. Sun, D. Xia, and C.-Y. Kao, "Active contours driven by local and global intensity fitting energy with application to brain MR image segmentation," *Computerized Med. Imag. Graph.*, vol. 33, no. 7, pp. 520–531, Oct. 2009.
[21] Y. Peng, F. Liu, and S. Liu, "Active contours driven by normalized local image fitting energy," *Concurrency Comput., Pract. Exper.*, vol. 26, no. 5, pp. 1200–1214, Apr. 2014.
[22] W. Zhao, X. Xu, Y. Zhu, and F. Xu, "Active contour model based on local and global Gaussian fitting energy for medical image segmentation," *Optik*, vol. 158, pp. 1160–1169, Apr. 2018.
[23] K. Saini, M. L. Dewal, and M. Rohit, "A fast region-based active contour model for boundary detection of echocardiographic images," *J. Digit. Imag.*, vol. 25, no. 2, pp. 271–278, Apr. 2012.
[24] X. Wang, D. Huang, and H. Xu, "An efficient local Chan–Vese model for image segmentation," *Pattern Recognit.*, vol. 43, no. 3, pp. 603–618, Mar. 2010.
[25] L. Fang, T. Qiu, Y. Liu, and C. Chen, "Active contour model driven by global and local intensity information for ultrasound image segmentation," *Comput. Math. Appl.*, vol. 75, no. 12, pp. 4286–4299, Jun. 2018.
[26] Z. Liang, W. Liu, and R. Yao, "Contrast enhancement by nonlinear diffusion filtering," *IEEE Trans. Image Process.*, vol. 25, no. 2, pp. 673–686, Feb. 2016.

[27] T. M. Silva Filho, B. A. Pimentel, R. M. C. R. Souza, and A. L. I. Oliveira, "Hybrid methods for fuzzy clustering based on fuzzy c-means and improved particle swarm optimization," *Expert Syst. Appl.*, vol. 42, nos. 17–18, pp. 6315–6328, Oct. 2015.
[28] M. F. Talu, "ORACM: Online region-based active contour model," *Expert Syst. Appl.*, vol. 40, no. 16, pp. 6233–6240, Nov. 2013.
[29] K. Ding, L. Xiao, and G. Weng, "Active contours driven by local pre-fitting energy for fast image segmentation," *Pattern Recognit. Lett.*, vol. 104, pp. 29–36, Mar. 2018.
[30] W. Tang, J. Hu, H. Zhang, P. Wu, and H. He, "Kappa coefficient: A popular measure of rater agreement," *Shanghai Arch Psychiatry*, vol. 27, no. 1, pp. 62–67, 2015.
[31] J. Xue, B. Wang, Y. Ming, X. Liu, Z. Jiang, C. Wang, X. Liu, L. Chen, J. Qu, S. Xu, X. Tang, Y. Mao, Y. Liu, and D. Li, "Deep learning–based detection and segmentation-assisted management of brain metastases," *Neuro-Oncol.*, vol. 22, no. 4, pp. 505–514, Apr. 2020.
[32] A. Myronenko, "3D MRI brain tumor segmentation using autoencoder regularization," in *Proc. CVPR*, Salt Lake City, UT, USA, Jun. 2018, pp. 311–320.

**YUZHEN CAO** received the Ph.D. degree from Tianjin University, in 2007. She is currently a Professor with Tianjin University. Her research interest includes biomedical signal detection and processing.

**JIAYONG MAO** received the B.S. degree from Tianjin University, in 2018, where he is currently pursuing the M.S. degree. His research interests include medical image processing and semantic segmentation.

**HUI YU** received the Ph.D. degree from Tianjin University, in 2003. He is currently an Associate Professor with Tianjin University. His research interests include medical image processing and biomedical signal processing.

**QINHAO ZHANG** received the B.S. degree from Shanghai University. He is currently pursuing the master's degree with Tianjin University. His research interests include image processing and image recognition.

**HUIQUAN WANG** received the Ph.D. degree from Tianjin University, in 2014. He is currently an Associate Professor with Tiangong University. His research interests include biomedical photonics, biomedical electronics, and biomedical signal processing.

**QUANLU ZHANG** received the B.S. degree from the Qinghai Union Workers College. His research interest includes neuroradiology.

**LINGFEI GUO** received the M.D. degree from Shandong University. He is currently a Professor with Shandong University. His research interest includes neuroradiology.

**FEI GAO** received the Ph.D. degree in radiology from Shandong University, Jinan, China, in 2012. He is currently a Neuroradiologist with the Shandong Medical Imaging Research Institute, Shandong University. His research interests include neuroimaging, magnetic resonance spectroscopy, and neuroradiology.